

# Direct Recycling at the Material Level: Unravelling Challenges and Opportunities through a Case Study on Spent Ni-Rich Layered Oxide-Based Cathodes

Maïke Michelle Gnutzmann, Ardavan Makvandi, Bixian Ying, Julius Buchmann, Marco Joes Lüther, Bianca Helm, Peter Nagel, Martin Peterlechner, Gerhard Wilde, Aurora Gomez-Martin, Karin Kleiner, Martin Winter, and Johannes Kasnatscheew\*

Direct recycling is a key technology for enabling a circular economy of spent lithium ion batteries (LIBs). For cathode active materials (CAMs), it is regarded as the tightest closed-loop and most efficient approach among current recycling techniques as it simply proceeds via re-lithiation and reconstruction of aged CAMs instead of separating them into elemental components. In this work, spent, i.e., morphologically and structurally decomposed CAM based on  $\text{LiNi}_{0.83}\text{Co}_{0.12}\text{Mn}_{0.05}\text{O}_2$  (NCM-831205) is restored by mimicking conditions of original CAM synthesis. After evaluating and optimizing the high-temperature duration for CAM restoration and subsequent washing procedure, the recycled CAM is shown to maintain poly-crystallinity and tap density, successfully recover specific surface area, lithium content, crystal structure in surface and bulk, while, however, only partly the original secondary particle size and shape. Though, comparable in initial 100 charge/discharge cycles with pristine CAM in lithium ion-cells, the subsequent increase in resistance and capacity fading remains a challenge. High temperature during recycling can be regarded as a key challenge on material level, as it not only promotes detrimental surface carbonate species from residual carbon black but also enhances cation disorder and micro-/nanoscopic porosity through oxygen release, likely in de-lithiated, thus less thermally stable regions of cycled NCM.

## 1. Introduction

With ever-increasing production volumes and lifetimes beyond 10 years,<sup>[1]</sup> the worldwide quantity of end-of-life (EoL) lithium ion batteries (LIBs), in particular from electric vehicles (EVs), is expected to reach from 3.6 to 5.3 million metric tons in 2030.<sup>[2]</sup> In order to meet legislative requirements such as the Battery Regulation in the EU,<sup>[3]</sup> reduce environmental and health risks, and minimize dependency on critical suppliers, efficient and effective recycling strategies are essential.<sup>[4]</sup>

Among the three main recycling techniques presented in Figure 1, hydro-metallurgical, pyro-metallurgical and direct recycling, the former two have been widely adopted on an industrial scale.<sup>[1]</sup> In hydro-metallurgical recycling, metal oxides of the positive electrode (= cathode) are leached in acids, and the corresponding metal salts recovered by

M. M. Gnutzmann, B. Ying, J. Buchmann, M. J. Lüther, A. Gomez-Martin, K. Kleiner, M. Winter, J. Kasnatscheew  
MEET Battery Research Center  
Institute of Physical Chemistry  
University of Münster  
Corrensstr. 46, 48149 Münster, Germany  
E-mail: [johannes.kasnatscheew@uni-muenster.de](mailto:johannes.kasnatscheew@uni-muenster.de)

M. M. Gnutzmann, J. Buchmann  
International Graduate School for Battery Chemistry  
Characterization  
Analysis  
Recycling and Application (BACCARA)  
University of Münster  
Corrensstr. 40, 48149 Münster, Germany  
A. Makvandi, M. Peterlechner, G. Wilde  
Institute of Materials Physics  
University of Münster  
Wilhelm-Klemm-Str. 10, 48149 Münster, Germany  
A. Makvandi, M. Peterlechner  
Karlsruhe Institute of Technology  
Laboratory for Electron Microscopy (LEM)  
Engesserstr. 7, 76131 Karlsruhe, Germany  
B. Helm  
Institute of Inorganic and Analytical Chemistry  
University of Münster  
Corrensstr. 28/30, 48149 Münster, Germany

 The ORCID identification number(s) for the author(s) of this article can be found under <https://doi.org/10.1002/aenm.202400840>

© 2024 The Author(s). Advanced Energy Materials published by Wiley-VCH GmbH. This is an open access article under the terms of the [Creative Commons Attribution](https://creativecommons.org/licenses/by/4.0/) License, which permits use, distribution and reproduction in any medium, provided the original work is properly cited.

DOI: 10.1002/aenm.202400840

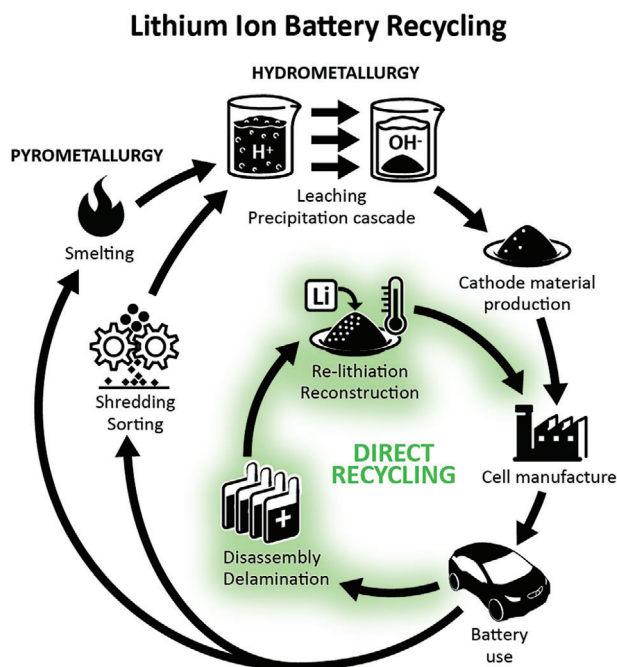


**Figure 1.** Schematics of state-of-the-art cathode recycling technologies for lithium ion batteries.

subsequent precipitation, while producing large amounts of wastewater.<sup>[1,5,6]</sup> Pyro-metallurgical recycling refers to the reduction of metal oxides in high-temperature furnaces and requires additional hydro-metallurgical post-processing to recover the transition metals (Co, Ni, Cu) from the resulting alloy; whereas lithium recovery remains challenging.<sup>[1,6]</sup> In contrast, direct recycling is interpreted as the reuse of battery components such as the cathode active material (CAM).<sup>[7]</sup> This beneficial closed-loop approach attracts attention from academia and is speculated to be already in early stages of commercialization. Direct recycling of the spent cathode comprises disassembly of the discharged cell, delamination/detachment of the cathode composite from the current collector, removal of binder/carbon black residues, and structural and morphological restoration via (re-)lithiation and high-temperature treatment (Figure 2), if a rather pure recycled material is targeted.<sup>[1,6–8]</sup> As a closed-loop approach, direct recycling not only inherently reduces energy consumption, greenhouse gas emissions, and water consumption but also provides a tremendous cost advantage over other recycling technolo-

gies and conventional raw material procurement from mines.<sup>[7]</sup> Net profits for direct recycling of  $\text{Li}[\text{Ni}_{0.8}\text{Co}_{0.1}\text{Mn}_{0.1}]\text{O}_2$  (NCM-811) waste produced in the UK are estimated to amount to  $\approx 3$  \$  $(\text{kWh})^{-1}$  in the UK (in-country recycling) and up to 10 \$  $(\text{kWh})^{-1}$  in China.<sup>[9]</sup>

Direct recycling has been demonstrated on several types of CAMs, e.g., lithium iron phosphate (LFP),<sup>[10]</sup> lithium nickel cobalt aluminum oxide (NCA),<sup>[11]</sup> lithium manganese oxide (LMO),<sup>[12]</sup> and  $\text{Li}[\text{Ni}_x\text{Co}_y\text{Mn}_z]\text{O}_2$  (NCM-xyz,  $x+y+z=1$ ),<sup>[13–15]</sup> applying various re-lithiation methods with different reported outcomes. Worth noting, predominant part of reported studies consider low- and mid-Ni NCM ( $x \leq 0.6$ ), likely as the result of being the dominant CAM in EV applications in recent years.<sup>[2]</sup> In 2015, Sloop et al.<sup>[13]</sup> patented a hydrothermal re-lithiation method for NCMs and published a study on NCM-523 and NCM-622 in 2019.<sup>[16]</sup> In 2018, Shi et al.<sup>[14]</sup> directly regenerated NCM-111 and NCM-523 via solid-state and hydrothermal direct recycling, showing a full restoration of phase purity and electrochemical performance in lithium metal cells. Also, re-lithiation in molten salts gains interest, as the increased mobility in solid solutions can upcycle NCMs in terms of stoichiometry and modify shapes, e.g., from poly-crystalline to “single-crystal”.<sup>[17,18]</sup> Nevertheless, to date, fundamental and comprehensive understanding of the impact on material level during direct recycling requires further investigations, in particular for Ni-rich NCM ( $x \geq 0.8$ ), being promising due to relatively higher specific energies and energy densities.<sup>[19]</sup>

A higher Ni-content is typically intertwined with a higher delithiation degree (=  $\text{Li}^+$  extraction) and capacity, but at the expense of structural stability and safety. Severe aging phenomena occur, such as impeded (de-)lithiation in the course of  $\text{Li}^+/\text{Ni}^{2+}$  cation mixing and transformation from layered to inactive rock-salt (NiO) phase, micro-crack formation, release of oxygen and dissolution of transition metals (TMs). The latter initiates a failure cascade, which can damage the negative electrode (= anode) in the course of electrode crosstalk, where TM can deposit on the anode and enhance local resistance, resulting in enhanced risk of Li deposition (e.g., via Li dendrites) and losses in active lithium.<sup>[20–23]</sup> To recover the original electrochemical performance, direct recycling needs to restore these degradation phenomena, rendering the Ni-rich CAMs particularly challenging. To the best of our knowledge, reports on solid-state direct recycling of charge/discharge cycling-aged Ni-rich NCM with  $x \geq 0.8$  are lacking.<sup>[24]</sup>

For reasons of a systematic and application-relevant study, investigation in lithium ion cells with commercial (= optimized) reference material including a defined spent material with known treatment history is essential. This work investigates solid-state re-lithiation as a direct recycling technique for  $\text{LiNi}_{0.83}\text{Co}_{0.12}\text{Mn}_{0.05}\text{O}_2$  (NCM-831205) at 80% state-of-health (SOH). Re-lithiation conditions mimic the synthesis of Ni-rich NCM from precursors, i.e., via lithium hydroxide monohydrate as (re-)lithiation agent, oxygen atmosphere and heating procedures with holding steps at intermediate (typically  $\approx 500$  °C) and high temperature (typically  $\approx 800$  °C),<sup>[25,26]</sup> thus can be applied by conventional CAM suppliers. Compared to conventional CAM synthesis, the CAM production via solid-state re-lithiation of spent material can relevantly reduce cost as the step for precursor formation via co-precipitation is not required, the duration for

P. Nagel  
Institute for Quantum Materials and Technologies (IQMT)  
Karlsruhe Institute of Technology (KIT)  
76021 Karlsruhe, Germany

P. Nagel  
Karlsruhe Nano and Micro Facility (KNMF)  
KIT  
Hermann-von-Helmholtz-Platz 1, 76344 Eggenstein-Leopoldshafen,  
Germany

M. Winter  
Helmholtz-Institute Münster  
IEK-12, Forschungszentrum Jülich GmbH, Corrensstr. 46, 48149 Münster,  
Germany

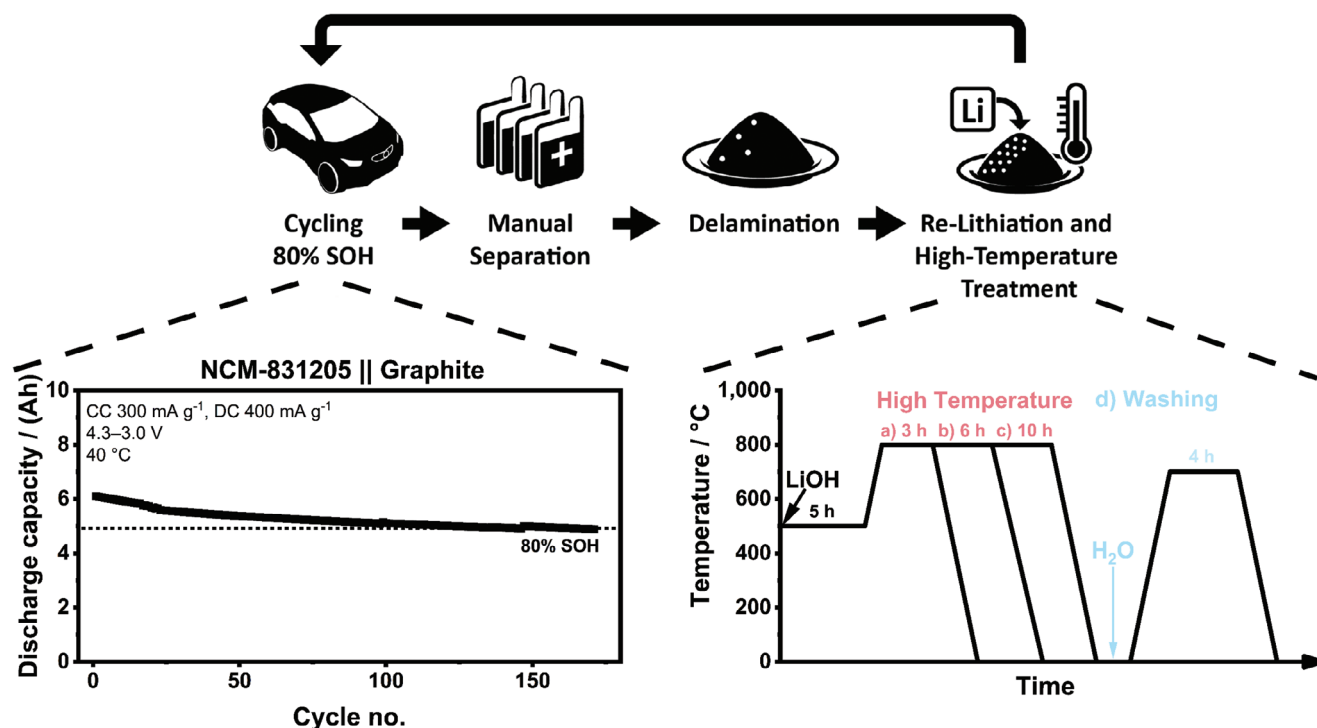


**Figure 2.** Direct recycling procedure of NCM-831205 || graphite multilayer pouch cells at 80% SOH, where a–c) duration of solid-state re-lithiation is varied, and d) the subsequent washing procedure is optionally applied. (CC and DC = charge and discharge current).

calcination at elevated temperature is shorter and lithium contents for (re-)lithiation lower.

Characterization of elemental composition, secondary particle size, shape, specific surface area, tap density and the evolution of NCM morphology during solid-state direct recycling is systematically investigated. Moreover, with the support of Warder titration, powder X-ray diffraction (PXRD), high-resolution transmission electron microscopy (HR-TEM), scanning transmission electron microscopy (STEM), electron energy-loss spectroscopy (EELS), and near edge X-ray absorption fine-structure spectroscopy (NEXAFS), the evolution of surface species, as well as bulk and surface crystal structure, is also comprehensively investigated and linked with electrochemical performance in NCM || Li metal and NCM || graphite lithium ion-cells. This work aims to benchmark and assess the solid-state direct recycling, diagnose remaining issues and finally pave the way for systematic R&D.

## 2. Results and Discussion

### 2.1. Direct Recycling Procedure

The direct recycling procedure of multilayer  $\text{Li}[\text{Ni}_{0.83}\text{Co}_{0.12}\text{Mn}_{0.05}]\text{O}_2$  (NCM-831205) || graphite pouch cells is illustrated in Figure 2. After fading to 80% of its original capacity, defined as state-of-health (SOH), the cells are disassembled in a discharged state in an argon-filled glovebox, the cathode coating delaminated from the aluminum foil by immersion in hot N-Methyl-2-pyrrolidone (NMP) and centrifuged to obtain cathode active material (CAM) powder (= Cycled). Afterwards, NCM is re-lithiated with lithium hydroxide monohydrate ( $\text{LiOH}\cdot\text{H}_2\text{O}$ )

via solid-state sintering in an oxygen atmosphere at high temperatures, similar to the typical synthesis route of Ni-rich layered oxides. Here, the samples are placed directly in a pre-heated muffle furnace at 500 °C to shorten the exposure time of the thermally unstable, cycled, and thus partially de-lithiated NCM (Figure S1, Supporting Information). The high-temperature step at 800 °C for 3, 6, or 10 h (= Recycled 3 h / 6 h / 10 h, Figure 2a–c) is finally conducted to complete re-lithiation and to reconstruct NCM. The washing step (= Recycled washed / not washed) is optionally applied to investigate the elimination of lithium-containing residues from the re-lithiation procedure, followed by high-temperature treatment to heal defects on water-sensitive Ni-rich-based CAM, eventually stemming from washing (Figure 2d). Details are described in the Experimental Section and in the Supporting Information.

Inductively coupled plasma optical emission spectroscopy (ICP-OES) results listed in Table S1 (Supporting Information) indicate a lithium loss of  $\approx 13\%$  in the aged NCM, and the lithium content is shown to be restored for all re-lithiation procedures.

### 2.2. Morphology

Commercial Ni-rich NCM has an optimized particle design in terms of secondary particle size and shape, specific surface area and tap density, contributing to energy density. For the commercial pristine NCM-831205, the scanning electron micrograph (SEM) in Figure 3a1 shows spherical secondary particles with a narrow size distribution. Surface species (Figure 3a2) can stem from synthesis or air exposure, although generally stored in a

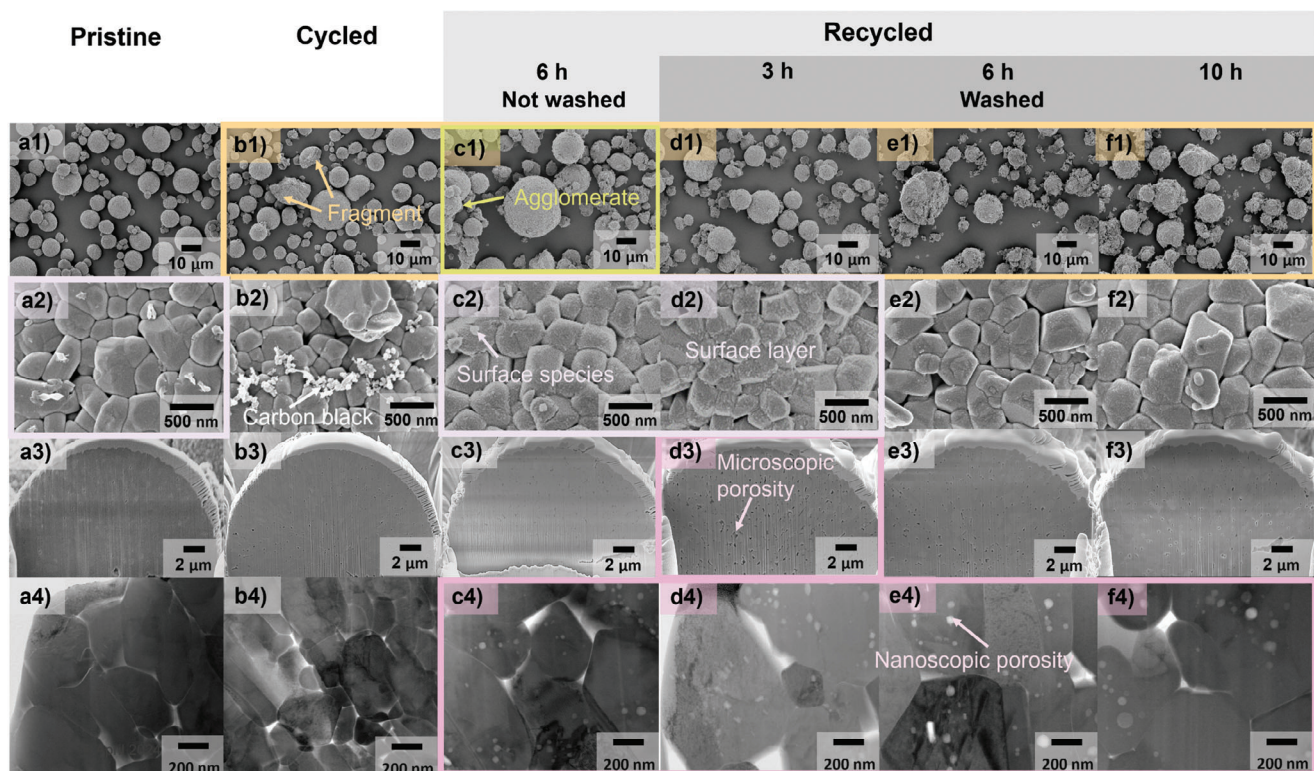


**Figure 3.** Images of NCM-831205 powder morphology, showing 1) and 2) top-view, 3) cross-sectional SEM, 4) cross-sectional BF-STEM of a) pristine, b) cycled, and c–f) directly recycled samples. Arrows indicate exemplary particle fragments in b1), an agglomerate in c1), surface species in c2), microscopic porosity in d3) and nanoscopic porosity in e4). Colored rectangles indicate where the respective phenomenon is observed.

dry atmosphere. Due to well-known micro-crack formation of NCM at high de-lithiation degrees,<sup>[21,22,26–28]</sup> and after delamination and centrifugation, some fragmented particles are observed (Figure 3b1) for cycled NCM. Fragmented particles in Figure 3c1–f1 demonstrate that thermal solid-state recycling cannot entirely recover these morphological defects. The SEM images also indicate fewer agglomerates and surface species after washing, facilitating electrode paste processing in NMP and accessibility to the inner pore network. For short high-temperature treatments (Recycled 3 h, washed; Figure 3d2), a surface layer is still present after the washing step but is removed completely for longer high-temperature treatments (Recycled 6 h / 10 h, washed; Figure 3e2,f2) and is further investigated by Warder Titration in the next section. Cross-sectional SEM images in Figure 3a3–f3 reveal an initially increased microscopic porosity between primary particles during solid-state re-lithiation, which decreases at longer high-temperature treatment. Complementary, cross-sectional bright-field scanning transmission electron micrographs (BF-STEM) in Figure 3a4–f4 clearly prove emerging nanoscopic porosity upon re-lithiation. Because cycled (= de-lithiated) NCM is unstable at  $T > 140$  °C (Figure S1, Supporting Information),<sup>[29]</sup> the increase in porosity on micro- and nanoscale could stem from oxygen release<sup>[30]</sup> when exposed to heat. In contrast to the microscopic porosity, intra-granular nanopores are assumed to be isolated and filled with trapped molecular oxygen. The internal pressure can stabilize the nano-pores,<sup>[31]</sup> therefore, there may be no reduction in nano-porosity observed in the course of the high-temperature treatment. The re-integra-

tion of oxygen is also conceivable. Whether a steady-state of forward (NCM decomposition) and backward reaction is reached, or whether the pores constantly grow and disappear, is not elucidated by the ex situ experiment. Further, only a small portion of one particle has been investigated, and more extensive studies are needed to provide representative evidence. Intra-granular nanopore surfaces are suggested to be critical as they aggravate the degradation of NCM during charge/discharge cycling by increasing oxygen loss, the formation of rock-salt regions, and strain-induced effects within the primary grains.<sup>[32]</sup>

The secondary particle size (circular-equivalent diameter) and shape as well as the specific surface area, are determined by static light scattering, dynamic image analysis and Krypton physisorption, respectively (Figure 4; Figures S2–S8, Table S2, Supporting Information). Pristine NCM-831205 particles with a size of  $\approx 10.5$   $\mu\text{m}$  ( $d_{50}$ ) and a narrow monomodal distribution have an average circularity of 0.917 and a specific surface area of  $\approx 0.47$   $\text{m}^2$   $\text{g}^{-1}$ . Particle cracking upon charge/discharge cycling and fragmentation during delamination reduce the particle size of the cycled material to  $\approx 9.9$   $\mu\text{m}$  ( $d_{50}$ ). The particle size of the recycled sample without a washing step increases to ( $d_{50}$ )  $> 14$   $\mu\text{m}$ , while average circularity and specific surface area decrease to 0.899 and  $\approx 0.38$   $\text{m}^2$   $\text{g}^{-1}$ , respectively, which can be associated with agglomerations according to SEM. The washing step dissolves surface species, thereby removing the “glue” between agglomerated particles, uncovering the surface, and increasing access to the inner pore network.<sup>[33]</sup> With the restoration of 6 h high-temperature treatment, an optimum can be reached with

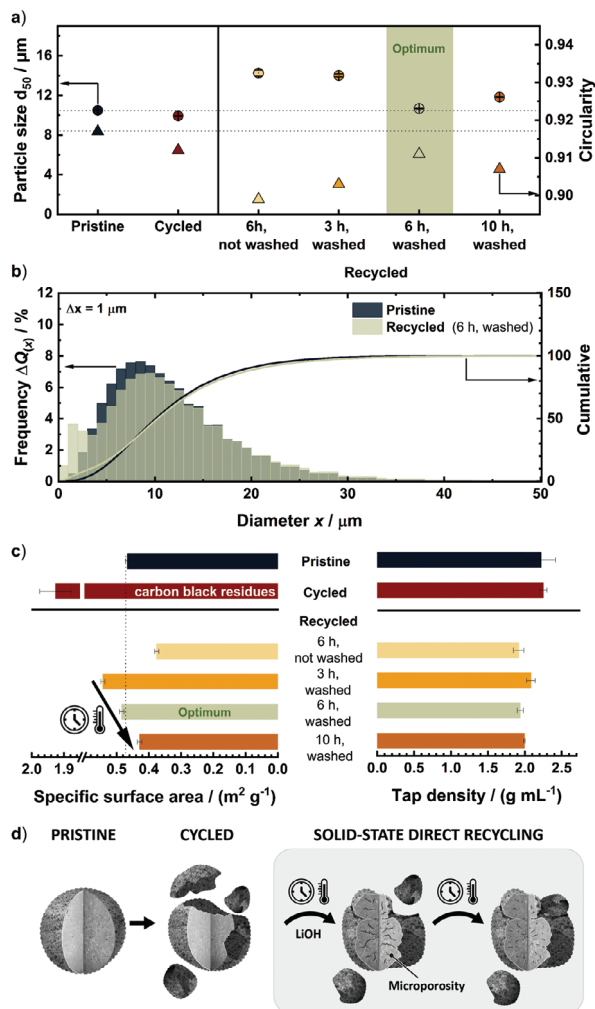


**Figure 4.** Morphological evolution of NCM-83 1205 powders. a) Particle size ( $d_{50}$ ) and average circularity, b) particle size distribution, c) specific surface area and tap density of the pristine, cycled, and directly recycled samples and d) summarizing scheme.

respect to the particle size ( $d_{50} = \approx 10.7 \mu\text{m}$ ), average circularity (0.911) and specific surface area ( $\approx 0.48 \text{ m}^2 \text{ g}^{-1}$ ). Despite similar mean particle sizes, the recycled sample (Recycled 6 h, washed) contains a larger fraction of small and less spherical particles (Figure 4a,b). During high temperatures, Ostwald ripening can occur, which claims inter- and intra-particle relocation for reasons of surface energy reduction,<sup>[34]</sup> resulting in a linear decrease in specific surface area (Figure 4c). Accordingly, particle enlargement is observed when raising the high-temperature duration from 6 to 10 h. Recycled 3 h, washed and Recycled 6 h, unwashed do not fit the trend, likely because of surface layer reasoned agglomerations, as seen by SEM analysis and titration results in the next section. Note that, contrary to nanoscale porosity, microscopic porosity is part of the inner pore network, therefore, accessible for krypton during physisorption measurements and to electrolyte in an electrochemical cell.

Particle shape, size and its distribution are crucial for tap density, thus energy density,<sup>[35]</sup> and is in the range of  $1.9\text{--}2.3 \text{ g cm}^{-3}$

for all samples, as depicted in Figure 4c. Despite similar tap densities, the impact of these particle-related parameter on other aspects remains unsolved, being important for measures, where morphology can relevantly change, e.g., recycling via molten-salt re-lithiation.<sup>[17]</sup>

### 2.3. Surface Species

Surface species on CAM can be detrimental for battery operation.<sup>[36,37]</sup> Given residual carbon black in the cycled sample and lithium hydroxide monohydrate as re-lithiation agent, the presence of lithium hydroxides and carbonates is suggested. According to their solubility in water ( $113$  and  $8.4 \text{ g L}^{-1}$  at  $20^\circ\text{C}$ ), the effectiveness of the washing step with excess water is investigated via Warder titration.<sup>[38]</sup> Figure 5a shows the titration curves, and Figure 5b and Table S3 (Supporting Information) list the resulting surface hydroxide and carbonate contents for the pristine as well as the unwashed and washed recycled samples. Indeed, the hydroxide content decreases from  $\approx 4300$  to  $\approx 1800 \text{ ppm}_{\text{NCM}}$  for washed NCM as well as the carbonate content from  $\approx 4500$  to  $\approx 2800 \text{ ppm}_{\text{NCM}}$  (Recycled 6 h, not washed vs Recycled 6 h, washed). Lithium carbonate melts and decomposes at significantly higher temperatures than lithium hydroxide ( $723$  and  $1300^\circ\text{C}$  vs  $423$  and  $924^\circ\text{C}$ , respectively) and dissipates after 1 h at  $800^\circ\text{C}$  during the synthesis of Ni-rich NCM.<sup>[39]</sup> Contrary to original NCM synthesis from rather pure hydroxide precursors, the residual carbon black in the cycled NCM during recycling raises the carbonate content at the beginning of

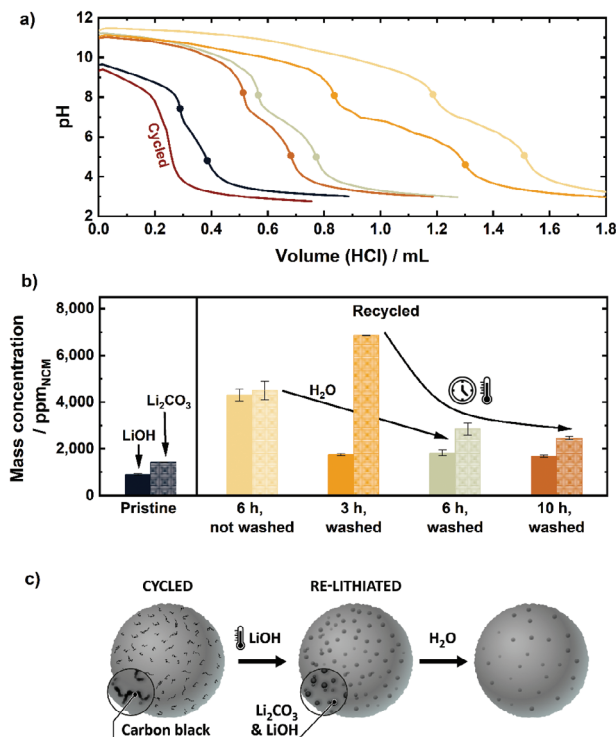


**Figure 5.** Data from Warder titration of NCM-83 1205. a) Titration curves with equivalence points indicated as dots, b) lithium hydroxide and carbonate content on the pristine, not washed and washed directly recycled samples, and c) schematic summary.

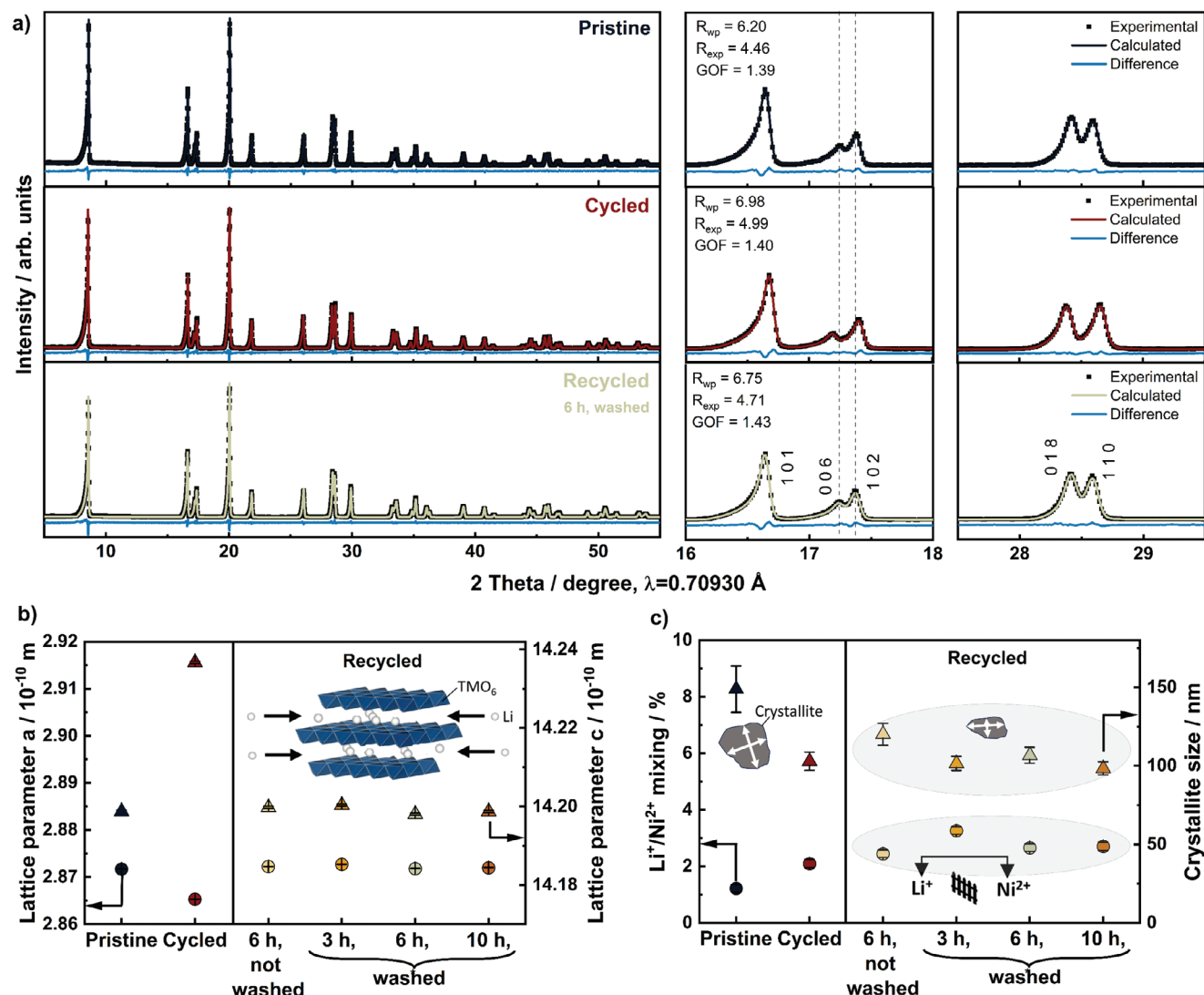


**Figure 6.** Evolution of NCM-831205 bulk crystal structure. a) PXRD patterns and Rietveld refinements of the pristine, cycled, and directly recycled samples, b) lattice parameters, c) Li<sup>+</sup>/Ni<sup>2+</sup> mixing and crystallite size determined by Rietveld refinement.

re-lithiation, requiring more than 3 h of high-temperature treatment for effective evaporation. The high carbonate content in Recycled 3 h, washed of  $\approx 6850$  ppm<sub>NCM</sub> is in line with the observed surface layer via SEM. Consistent with previous reports,<sup>[36,38]</sup> surface species are also observed on the pristine sample ( $\approx 890$  and  $\approx 1450$  ppm<sub>NCM</sub> for LiOH and Li<sub>2</sub>CO<sub>3</sub>, respectively), while they are even lower for the cycled sample, likely in the course of chemical reactions and decompositions with electrolyte during charge/discharge cycling.<sup>[40]</sup> To most effectively achieve a surface purity comparable to the pristine material the carbon black content should be reduced prior to re-lithiation. Alternatively, an increased amount of deionized water relative to NCM from 1:1 to 3:1 wt% (Figure S9, Supporting Information) in fact reduces the surface species. However, more excess water further promotes surface defects<sup>[41]</sup> and without complementary adjustments to the post-annealing step, no improvement in electrochemical performance is evident (Figure S10, Supporting Information).

Binder residues are expected to be present in Cycled (Figure S11, Supporting Information). Therefore, after re-lithiation the metal fluoride concentration is increased to  $2.1 \pm 0.8$  at.% (Pristine:  $0.7 \pm 0.1$  at.%) on the surface of the recycled sample (Recycled 6 h, washed; Figure S13, Supporting Information). Nevertheless, diffusion of the surface fluorine to the bulk during the high temperatures of the re-lithiation process is not detected via energy dispersive X-ray spectroscopy in a scanning transmission electron microscope (EDX-STEM, Figure S14, Supporting Information).

#### 2.4. Crystal Structure

The CAM crystal structure is investigated via powder X-ray diffraction (PXRD, Figure 6a; Figures S15–S17, Supporting Information) and Rietveld refinement (Figure 6b,c; Table S4, Supporting Information). All diffraction patterns can be indexed to

a single-phase hexagonal  $\alpha$ -NaFeO<sub>2</sub> structure, belonging to the space group  $R\bar{3}m$  (no. 166). The clear splitting of the reflection doublets, described by the lattice planes (006)/(102) and (108)/(110), indicates a highly ordered layered structure.<sup>[25]</sup> Reflection positions are related to lattice parameters, and the position of the 006 reflection represents an indirect measure for the distance in the  $c$ -direction between the lithium and  $TM$  slabs. It is shifted to lower scattering angles for the cycled sample, as delithiation by  $\approx 13\%$  increases electrostatic repulsion between the adjacent oxygen slabs and, thus, expands the interlayer distance and the lattice parameter  $c$  in Figure 6b. In parallel, the oxidized  $TMs$  in the de-lithiated state, exhibiting smaller ionic radii themselves and reducing the effective ionic radius of the oxides by withdrawing electron density, contract the crystal along the crystallographic  $a$ - and  $b$ -axis (Figure 6b).<sup>[42]</sup> The lattice parameters are restored to original (pristine) values for the recycled samples, proving complete re-lithiation into the crystal structure. Due to similar radii of Ni<sup>2+</sup> (0.69 Å) and Li<sup>+</sup> (0.76 Å), Ni<sup>2+</sup> can diffuse into the lithium layer (Wyckoff 3b) in de-lithiated states during charge/discharge, whereas Li ions occupy the vacant  $TM$  sites (Wyckoff 3a) of the rhombohedral structure, literature-known as Li<sup>+</sup>/Ni<sup>2+</sup> mixing.<sup>[43]</sup> High cation mixing decreases electrochemical performance because lithium movement within the lithium slab is impeded due to both, Ni<sup>2+</sup> as obstacle and locally minimized Li slab in the course of increased oxide attraction of the harder Ni<sup>2+</sup>.<sup>[22,44]</sup> The Li<sup>+</sup>/Ni<sup>2+</sup> mixing shown in Figure 6c is determined by the refined occupancy of Ni in the Li sites (Wyckoff 3b) and is enhanced for the cycled sample ( $2.1 \pm 0.2\%$ ) compared to pristine ( $1.2 \pm 0.1\%$ ). The recycling procedures result in slightly higher disorders (2.4–3.3%), among which  $\geq 6$  h show lowest values of  $\approx 3\%$ ; in accordance with reports on laboratory synthesized Ni-rich NCMs.<sup>[25,26]</sup> Results are similar to Shi et al.,<sup>[14]</sup> who demonstrated increased cation mixing from 3.39% to 5.10% for NCM-523 when charged to 4.5 V and a decrease to only 4.28% after solid-state re-lithiation. Based on in-depth investigations of NCM-811 synthesis via synchrotron radiation, cation mixing can be controlled by temperature adjustments and cooling rate in the solid-state re-lithiation procedure.<sup>[25]</sup>

Volume-averaged crystallite sizes are determined as angular dependent sample contribution to the reflection broadening, using integral breadths, and are depicted in Figure 6c. Crystallite sizes of the Ni-rich NCM decrease from  $149 \pm 15$  to  $103 \pm 6$  nm after charge/discharge cycling, possibly due to anisotropic volume changes during (de-)lithiation.<sup>[28]</sup> The presented re-lithiation procedure does not restore initial crystallite sizes. As the previously mentioned nanovoids are presumably stabilized and tend to grow by oxygen gas expansion they could suppress average crystallite size growth, while the overall particle still grows. Nevertheless, for higher crystallite size, treatment at a higher temperature ( $>800$  °C) can be an effective approach,<sup>[31,45,46]</sup> although enhancing Li<sup>+</sup>/Ni<sup>2+</sup> mixing for Ni-rich NCM above 850 °C.<sup>[39]</sup>

The crystal and electronic structure in the bulk and at the surface are examined via high-resolution transmission electron microscopy (HR-TEM), electron energy loss spectroscopy within a scanning transmission electron microscope (EELS-STEM) and complementary near edge X-ray absorption fine-structure spectroscopy (NEXAFS). HR-TEM images and the corresponding Fast Fourier Transform (FFT) patterns in Figures S18–S23 (Supporting Information) confirm a layered crystal structure ( $R\bar{3}m$ ) in

the bulk of all samples. Surface phase changes are known to occur in Ni-rich NCMs during charge/discharge, synthesis and storage.<sup>[36,47]</sup> In Figure 7a, a dense rock-salt structure belonging to the space group  $Fm\bar{3}m$  (no. 225) can be observed at the surface of cycled materials and partially also on pristine materials (Figure S18, Supporting Information). The directly recycled samples differ in terms of phase purity of the surface region (Figures S20–S23, Supporting Information). The particle fraction of Recycled 6 h, washed in Figure 7a and Figure S22 (Supporting Information), shows a layered structure at the surface, indicating a successful surface reconstruction from the rock-salt to a layered phase (Figure 7a scheme) which is consistent with previous reports.<sup>[14,48]</sup> The oxidation states of the  $TMs$  and oxygen in the bulk and at the surface, playing a key role in phase evolution and cation mixing, are probed by EELS-STEM and NEXAFS, as depicted in Figure 7b and Figures S24–S26 (Supporting Information). In contrast to the pristine, the Ni L edge core-loss EELS spectrum of the bulk of the cycled sample reveals a chemical shift of the L<sub>3</sub> (and L<sub>2</sub>) peak to higher energies, while a slight decrease of the N<sub>1</sub>/N<sub>2</sub> peak ratio in the bulk of the cycled material is observed in the NEXAFS fluorescence yield (FY) Ni L edge. These observations correspond to a higher oxidation state of Ni<sup>[47,49]</sup> for maintaining charge neutrality in the lithium-deficient material. This higher Ni oxidation state is restored by direct recycling, as supported by EELS-STEM and NEXAFS FY. Regarding bulk Co, NEXAFS FY shows no change in the oxidation state, while EELS-STEM hints at minor, possibly negligible, oxidation in the bulk of the cycled material (Figures S24 and S25, Supporting Information). The pre-peak feature, i.e., O<sub>1</sub> and O<sub>2</sub> peaks in the FY O K NEXAFS edge, are related to the hybridization of O 2p states with  $TM$  3d states (= covalency, s-type interactions).<sup>[49]</sup> The O<sub>3</sub> peak might be assigned to Hubbard bands. Unravelling the origin of the high intensity in the pristine (commercial) material requires further studies, but it might be due to an electron-withdrawing effect from a protective coating or doping (substitution).<sup>[50]</sup> Despite NEXAFS FY confirming no changes in the oxidation states of bulk Co and Mn (Figures S25 and S26, Supporting Information) and a complete restoration of the oxidation state of bulk Ni, the extent of hybridization is only partially recovered by direct recycling which might also go back to a surface treatment of the commercial material.

Toward the surface, the L<sub>3</sub> peak is slightly shifted to lower energies in case for Ni and strongly for Co in the EELS spectrum, and the N<sub>1</sub>/N<sub>2</sub>, as well as C<sub>1</sub>/C<sub>2</sub> peak ratio in NEXAFS Ni L edge and Co L edge total electron yield (TEY) spectra are increased for all samples. Complementary, the pre-peak in the TEY O K edge decreases in intensity, proving a surface reduction layer (SRL, e.g., an oxygen depleted spinel or rock salt structure) for all samples of at least the thickness of the probing depth of NEXAFS TEY measurements ( $\approx 10$  nm). Cross-sectional EELS-STEM can probe the surface region without the influence of surface layers (surface species and cathode electrolyte interphase (CEI)), while NEXAFS accumulates the signal over a certain depth (FY,  $\approx$  a few hundred nm, TEY,  $\approx 10$  nm), becoming more complex for samples with differing surface layers. For instance, the presence of the O<sub>4</sub> peak in the NEXAFS TEY spectrum of the directly recycled sample is assigned to surface impurities such as Li<sub>2</sub>CO<sub>3</sub>,<sup>[51]</sup> aligning with results from Warder titration. Further, an increase in hybridization in the NEXAFS TEY O K edge and a

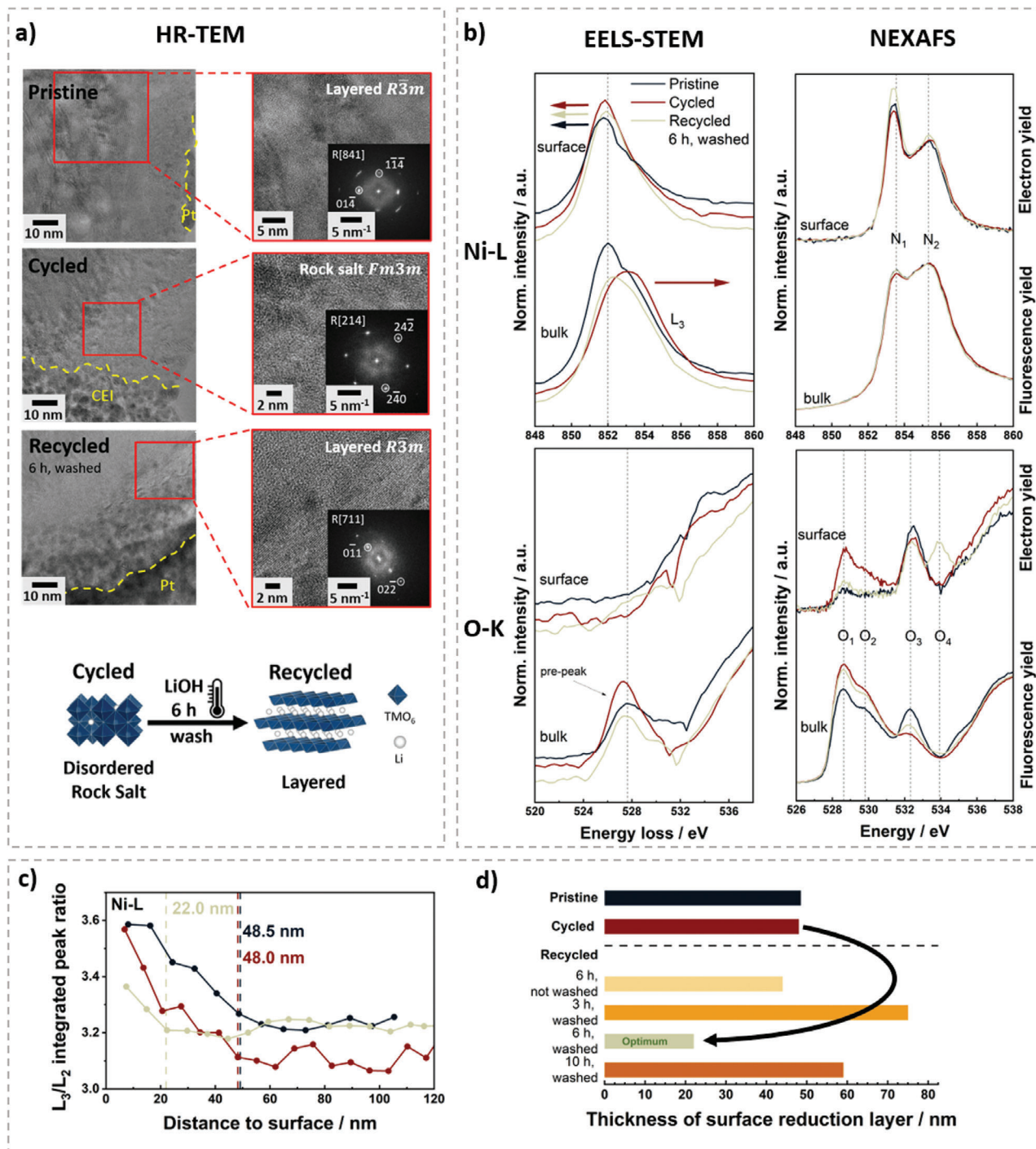


**Figure 7.** Evolution of NCM-831205 surface crystal structure. a) HR-TEM images, the corresponding FFT patterns and scheme of phase reconstruction at the surface upon optimal re-lithiation and high-temperature treatment conditions, b) Ni L edge and O K edge core-loss EELS and NEXAFS (FY and TEY) spectra, c) Ni L<sub>3</sub>/L<sub>2</sub> integrated peak ratio, and d) thickness of surface reduction layer.

reduction in the N<sub>1</sub>/N<sub>2</sub> ratio is detected for the cycled NCM surface in comparison to the pristine which could be attributed to the slightly de-lithiated state<sup>[52]</sup> but not via EELS-STEM. The loss of the Ni–O hybrid states (peak O<sub>1</sub> and O<sub>2</sub>) and an increase in the O<sub>3</sub> peak as well as in the N<sub>1</sub>/N<sub>2</sub> ratio after direct recycling suggests (partial) restoration of the surface region. EELS-STEM,

as well as HR-TEM measurements, are generally performed on a small portion of the sample (typically <1 μm x <1 μm on one to a few particles), and therefore, results and interpretations are less representative for the overall structure. Moreover, the materials are cut into lamella which introduced energy into the sample and changes in the chemistry, especially on the surface of the lamella,

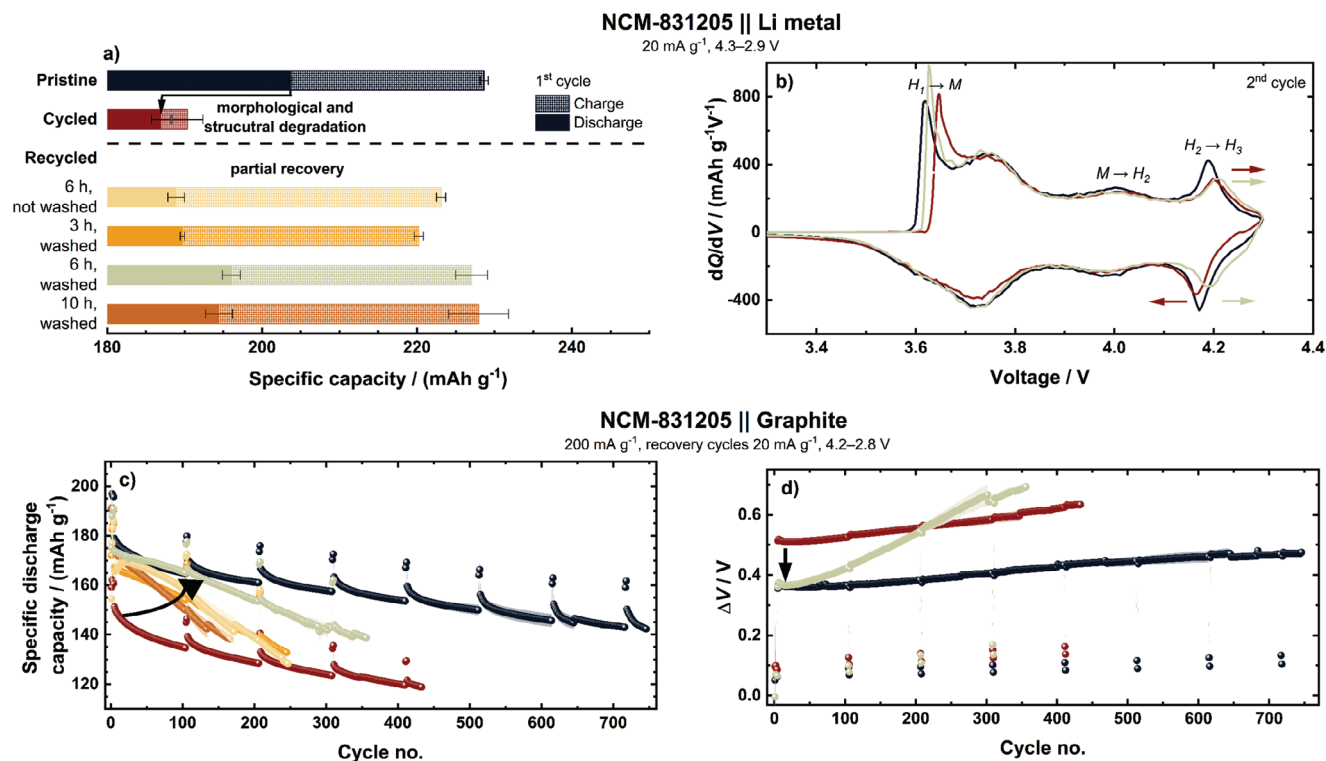


**Figure 8.** Galvanostatic data of pristine, cycled, and directly recycled NCM-831205 cathodes. a) First cycle specific capacity, and b) second cycle differential capacity ( $dQ/dV$ ) versus voltage plots in NCM || Li metal cells at 20 mA g<sup>-1</sup>, c) specific discharge capacity and d) difference between average charge and discharge voltages ( $\Delta V$ ) of continuous charge/discharge cycling in NCM || graphite lithium ion-cells at 200 mA g<sup>-1</sup>. Every 100 cycles two cycles at 20 mA g<sup>-1</sup> are performed. Error bars represent the standard deviation of three cells studied for each sample. N/P-ratio: 1.15:1.00, conventional electrolyte (1 M LiPF<sub>6</sub> in 3:7 vol.% EC/EMC + 2 wt% VC).

cannot be completely excluded. NEXFAS is included in the analysis, as it probes several milligrams of material (beamspot 0.6 mm x 1.5 mm on the electrode), being more representative and resulting in a higher signal-to-noise ratio. For EELS-STEM measurements, the L<sub>3</sub>/L<sub>2</sub> integrated peak ratio is associated with the oxidation states of transition metals and can determine the SRL thickness.<sup>[47,53]</sup> In Figure 7c and Figure S27 (Supporting Information), the L<sub>3</sub>/L<sub>2</sub> integrated peak ratio of the Ni L edge increases toward the surface for all samples, corresponding to lower oxidation states. This is confirmed by the differences in the TEY versus FY mode data of the Ni L<sub>2,3</sub> and O K edge (decreasing peaks at 528–529 eV and 530 eV in the TEY, Figure 7b; Figure S24, Supporting Information). In agreement with results from HR-TEM, Recycled 6 h, washed has the thinnest SRL (≈22 nm). The SRLs of pristine and cycled samples are ≈48 nm thick. While this creates the impression that charge/discharge cycling does not induce further rock-salt formation, the observation is more likely due to the heterogeneous character of the SRL, even within one primary particle.<sup>[47,54]</sup> As Figure 7d shows, short high-temperature treatments (Recycled 3 h, washed) lead to very thick SRLs, indicating that rock-salt phases initially increase before they are reduced again over time at high temperatures. This is consistent with the thermal instability of de-lithiated NCM and the nanoscopic porosity observed in the directly recycled samples, which can be attributed to oxygen loss and associated with the phase transformation from layered to rock-salt phase. Long high-temperature treatments (Recycled 10 h, washed), on the other side, also lead

to thicker SRLs, as the enhanced lithium loss at the surface region induces Ni<sup>2+</sup> diffusion from the bulk to the vacant sites at the surface.<sup>[25,39,47]</sup>

## 2.5. Electrochemical Characterization

Initial charge (= de-lithiation of the positive electrode) and discharge (= lithiation of the positive electrode) capacities of NCM || Li cells at 20 mA g<sup>-1</sup> are shown in Figure 8a. The first specific charge capacity of the pristine sample of 229 ± 1 mAh g<sup>-1</sup> is lowered to 190 ± 2 mAh g<sup>-1</sup> for the cycled NCM, while the first specific discharge capacity is only lowered by 17 mAh g<sup>-1</sup>. This implies capacity gain via electrochemical re-lithiation during discharge, while the residual capacity difference to pristine can be attributed to structural and morphological decompositions. The recycled samples show similar first charge capacities as the reference (between ≈220 and 228 mAh g<sup>-1</sup>), but lower first discharge capacities. Among the recycled samples, Recycled 6 h, washed performs best with 196 ± 1 mAh g<sup>-1</sup> compared to pristine with 203.7 ± 0.2 mAh g<sup>-1</sup>.

Figure 8b and Figure S28 (Supporting Information) show the second cycle differential capacity ( $dQ/dV$ ) as a function of cell voltage in NCM || Li metal cells at 20 mA g<sup>-1</sup>. The first cycle voltage profile and the corresponding  $dQ/dV$  versus V plot are shown in Figure S29 (Supporting Information). A kinetic hindrance region in the H<sub>1</sub> phase, H<sub>1</sub>-M (≈3.6 V), M-H<sub>2</sub> (≈4.0 V),

and  $H_2-H_3$  ( $\approx 4.2$  V) phase transition peaks can be identified.<sup>[20,55]</sup> H refers to hexagonal phases, numbered according to their order of appearance during de-lithiation of the cathode, and M to a monoclinic phase.<sup>[45]</sup> The onset of the  $H_1-M$  phase transition in the second charge is shifted to higher cell voltages for the cycled compared to pristine and recycled NCM, indicating kinetically more hindered/resistive de-lithiation.<sup>[56]</sup> The  $H_2-H_3$  phase transition for the cycled NCM is shifted to higher cell voltages during charge and respectively to lower during discharge in the course of cell polarization and overvoltage, likely from, e.g., CEI residues and micro-cracks.<sup>[26]</sup> The  $H_2-H_3$  phase transition of the recycled samples, however, occurs at higher cell voltages during charge and discharge, implying changed transition thermodynamics.<sup>[45]</sup> This could be related to the increase in  $Li^+/Ni^{2+}$  cation mixing in the recycled samples, as the decreased lithium interslab thickness in the  $H_3$  phase is expected to be less favorable in the presence of  $Ni^{2+}$  ions in the interslab.<sup>[28,45]</sup> The same asymmetric shift in voltage for the  $H_2-H_3$  phase transition occurs, e.g., with Mg substituted Ni-rich NCMs, as the electrochemically inactive Mg serves as an even more effective interslab pillar than the active Ni.<sup>[26,57]</sup> Though, the cycled NCM shows also an increased  $Li^+/Ni^{2+}$  cation mixing, but kinetic hindrances likely interfere with the thermodynamic effect.

The reduced discharge capacities of the directly recycled samples can be mainly associated to a decrease in peak intensity related to the  $H_2-H_3$  phase transition. Figure S30 (Supporting Information) shows the specific discharge capacities at specific discharge currents from 20 mA g<sup>-1</sup> ( $\approx 0.1C$ ) to 600 mA g<sup>-1</sup> ( $\approx 3C$ ) and increasing upper operating cell voltages (4.3, 4.4, and 4.5 V) to assess rate capability and stability at high-voltage operation. Specific charge currents are limited to 40 mA g<sup>-1</sup> to minimize high surface area lithium (HSAL) on the lithium metal anode. The rate capability is discussed in the Supporting Information. The pristine and cycled samples exhibit similar stability to high-voltage operation, while all recycled samples show higher capacities and retention up to 4.4 V. Among the recycled samples and in line with the superior morphological and surface characteristics shown in the previous sections, the sample Recycled 6 h, washed displays the best electrochemical performance in NCM-831205 || Li metal cells in terms of (initial) discharge capacity and cycle stability at high-voltage operation.

The specific discharge capacities of the pristine, cycled and optimized directly recycled sample Recycled 6 h, washed in NCM-831205 || graphite lithium ion-cells (4.2–2.8 V) are  $195.7 \pm 0.1$  mAh g<sup>-1</sup>,  $161 \pm 2$  mAh g<sup>-1</sup>, and  $190.8 \pm 0.2$  mAh g<sup>-1</sup>, respectively. Thus,  $\approx 85\%$  of the lost capacity could be recovered. Figure 8c shows differences in the charge/discharge cycling between the pristine, cycled and directly recycled samples. The pristine and cycled samples reach capacity retentions of 92.1% and 89.4% after 100 cycles and 88.0% and 81.7% after 300 cycles, respectively. Among the directly recycled samples, Recycled 6 h, washed does not only exhibit the highest discharge capacities, exceeding the pristine material for over 50 cycles, but also the best capacity retention, reaching 95.0% after 100 cycles and 81.6% after 300 cycles. Without washing, NCM cannot reach the full capacity in the first cycles but shows a recovery afterwards, consistent with a previous report from Bi et al.<sup>[58]</sup> Thus, more extensive washing or thorough pre-removal of carbon black during delamination is expected to further improve long-term stability. Short

high-temperature treatments (3 h) lead to lower capacities during the whole cycle life, possibly due to the high content of surface carbonates with low Li ion conductivity. Long high-temperature treatments (10 h), on the other side, lead to a tremendous increase in capacity fading, which might be related to impeding rock-salt phases. Complementary, in Figure 8d, the voltage hysteresis, determined by the difference between the average charge and discharge voltages ( $\Delta V$ ), of the recycled material is similar to that of the pristine material at the beginning but severely increases and gets even higher than untreated cycled NCM. Morphological, structural, and surface analysis of the pristine and directly recycled Ni-rich NCM in the previous sections suggest an enhanced micro-crack formation due to nanoscopic porosity, increased  $Li^+/Ni^{2+}$  mixing and side effects from residual surface species. Table S5 (Supporting Information) lists additional electrochemical data, and Figures S33 and S34 (Supporting Information) show normalized capacities, Coulombic efficiencies  $C_{\text{eff}}$  and accumulated specific energies.

### 3. Conclusion

In this work, direct recycling of Ni-rich NCM, here  $LiNi_{0.83}Co_{0.12}Mn_{0.05}O_2$  (NCM-831205), from spent LIB cells at 80% state-of-health (SOH) is optimized and investigated from a materials point of view.

After cell disassembly and delamination, the aged and partially fragmented NCM is recovered and reconstructed via solid-state re-lithiation, high-temperature treatment and a washing step. Pristine-original specific surface area, tap density, layered surface and lithium content are obtained, as revealed by krypton physisorption, high-resolution transmission electron microscopy (HR-TEM), electron energy-loss spectroscopy (EELS) and inductively coupled plasma optical emission spectroscopy (ICP-OES). However, as shown by scanning electron microscopy (SEM), dynamic light scattering, powder X-ray diffraction (PXRD) and bright-field scanning transmission electron microscopy (BF-STEM), original particle size and shape are not entirely restored,  $Li^+/Ni^{2+}$  mixing is slightly increased, crystallite size is reduced and a nanoscopic porosity emerged.

Morphological properties and surface crystal structure are shown to strongly depend on the duration of the high-temperature step and the amount of lithium source; in this work 6 h at 800 °C is demonstrated to be optimal. The washing step is shown to effectively remove surface hydroxides and carbonates stemming from reactions of residual carbon black and the lithiation agent as proven by Warder titration and SEM. Overall, the performance in NCM || graphite cells can compete with pristine NCM within the first  $\approx 100$  cycles. The capacity decay afterwards requires further research and development efforts and is speculated to be intertwined with increased  $Li^+/Ni^{2+}$  mixing and nanoporosity, which may lead to more cracking, increase in surface area, transition metal dissolution and crosstalk phenomena. Figure 9 schematically summarizes the remaining and addressable challenges for direct recycling on material level.

The presented direct recycling mimics the original synthesis of pristine NCMs<sup>[25,26]</sup> and is therefore potentially suitable for industrial manufacturing processes. However, the cycle life needs to be addressed and other re-lithiation methods re-considered, as the thermal treatment during re-lithiation is concluded to be

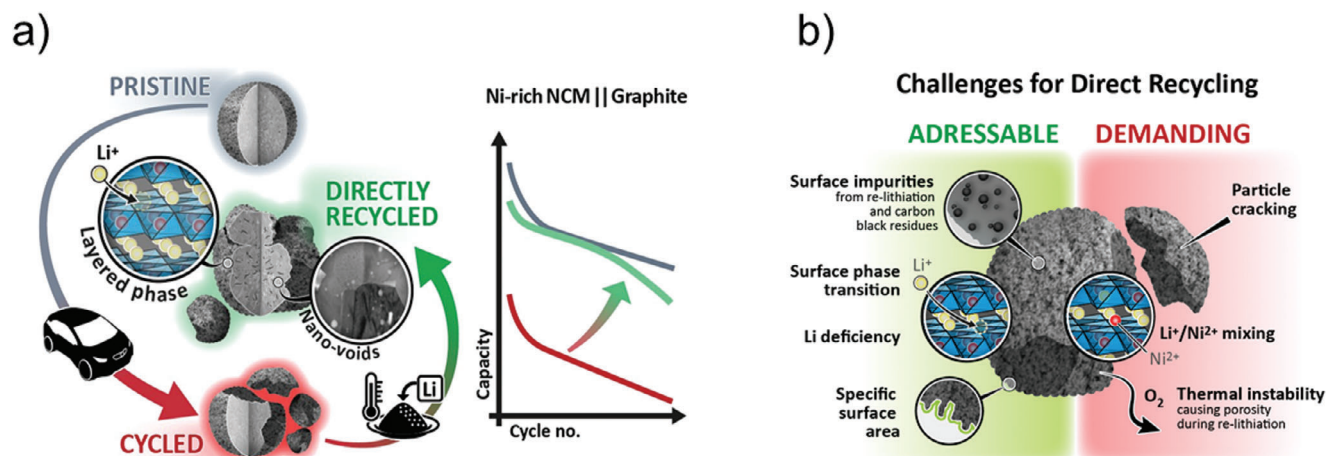


**Figure 9.** a) Scheme of solid-state direct recycling of Ni-rich NCM and respective performance in NCM || graphite cells showing the capacity recovery in initial cycles ( $\approx 100$ ). b) Manageable aspects and remaining/emerging challenges for direct recycling on material level identified in this work, demanding further research and development.

a key challenge. The thermal treatment has been shown to initiate detrimental side-effects not only including surface impurities from residual carbon black, but also enhanced  $\text{Li}^+/\text{Ni}^{2+}$  mixing and nanoscopic porosity, likely as the result of the locally delithiated, thus thermally instable regions within cycled NCM.

#### 4. Experimental Section

The dry room has a dew point of at least  $-50\text{ }^\circ\text{C}$  (relative humidity of  $<0.3\%$ ).

**Production and Charge/Discharge Cycling of Pouch Cells for the Generation of Spent Material:** A detailed description can be found in the Supporting Information.

**Direct Recycling of Cathode Active Material: Dismantling, Delamination, Re-Lithiation and High-Temperature Treatment:** Charge/Discharge cycled multilayer pouch cells were deeply discharged by an Ohmic resistance and dismantled in an argon-filled glovebox for safety reasons.<sup>[59]</sup> Moreover, deep discharge supports higher Li recovery rates for direct cathode recycling.<sup>[60]</sup> The cathode sheets were washed with dimethyl carbonate (DMC), transferred to a dry room, cut in small pieces and stirred in NMP at  $80\text{ }^\circ\text{C}$  for 2 h to delaminate the electrode coating from the aluminum current collector. The suspension was decanted in centrifuge tubes, leaving blank aluminum foil, and centrifuged at  $2000\text{ g}$  for 1 min 30 s. To remove binder residues and as much of the carbon black as possible, the precipitate was washed three times by adding fresh NMP, re-establishing a suspension through thorough vortexing, and subsequent centrifugation. After drying in a Büchi B-585 glass drying oven under reduced pressure ( $<5 \cdot 10^{-2}$  bar) at  $80\text{ }^\circ\text{C}$  for 12 h, the obtained powder was carefully ground in an agate mortar (this sample was referred to as Cycled).

The cycled active material was re-lithiated by thermal solid-state re-lithiation with or without a subsequent washing step. It was mixed homogeneously by mortar and pestle with ball-milled lithium hydroxide monohydrate ( $\text{LiOH} \cdot \text{H}_2\text{O}$ , 98%, Fisher Chemical) in a lithium/TM molar ratio of 1.03:1.00 or, for the samples which were to be washed, 1.06:1.00 for total masses of  $\approx 4\text{--}5\text{ g}$ . Excess of lithium was employed and optimized to cope for lithium losses during the decomposition of binder and carbon black residues and at high temperatures.<sup>[7,61]</sup> A higher excess of lithium was chosen for the samples to be washed, as this may be beneficial.<sup>[62]</sup> In addition, a small excess of lithium was shown to be beneficial for discharge capacities and cycle life of NCMs.<sup>[63]</sup> Samples were pre-treated above the melting point of lithium hydroxide ( $423\text{ }^\circ\text{C}$ ) at  $500\text{ }^\circ\text{C}$  for 5 h, thus, enabling lithium diffusion into the lithium-deficient NCM structure followed

by a high-temperature step at  $800\text{ }^\circ\text{C}$  for 3, 6, or 10 h. Because of the instability of lithium-deficient NCM at elevated temperatures (Figure S1, Supporting Information) leading to enhanced rock-salt formation,<sup>[29]</sup> samples were directly put into the pre-heated muffle furnace at  $500\text{ }^\circ\text{C}$ , limiting the time of exposure to heat before re-lithiation. Optionally, the obtained powder was washed in  $\leq 1:1$  wt% deionized water/NCM to remove residual surface species from re-lithiation and was post-treated at  $750\text{ }^\circ\text{C}$  for 4 h to heal surface defects stemming from the exposure to water.<sup>[64]</sup> All heating procedures were performed in a muffle furnace (Nabertherm GmbH, Lilienthal, Germany) under oxygen flow ( $75\text{ L h}^{-1}$ ) and with a heating and cooling rate of  $5\text{ }^\circ\text{C min}^{-1}$ . Obtained powders were ground carefully by mortar and pestle to reduce agglomerations of secondary particles and were referred to as Recycled 6 h, not washed, Recycled 3 h, washed, Recycled 6 h, washed, and Recycled 10 h, washed. The effect of variations of the Li/TM ratio and the temperature during re-lithiation on the electrochemical performance of NCM || Li metal cells are shown in Figures S31 and S32 (Supporting Information).

**Material Characterization:** For stoichiometry determination, samples were digested in reversed aqua regia (nitric acid and hydrochloric acid, 3:1) using a microwave system (Multiwave 7000, AntonPaar, Graz, Austria). Inductively coupled plasma optical emission spectroscopy (ICP-OES) measurements were performed using an ARCOS (Spectro Analytical Instruments GmbH, Kleve, Germany) equipped with a Scott spray chamber, a cross-flow nebulizer and a radial positioned plasma torch. The following emission lines were observed during analysis: Li (670.780 nm), Ni (221.648, 231.604, 232.003 nm), Co (228.616, 237.862, 238.892 nm), Mn (257.611, 259.373, 403.076 nm), Al (176.641, 394.401, 396.152 nm). The method and further parameters were adapted from Vortmann-Westhoven et al.<sup>[65]</sup> and Evertz et al.<sup>[66]</sup> The measurement was repeated three times.

The powder's thermal stability was investigated by differential scanning calorimetry (DSC), using hermetic aluminum pans in a DSC Q2000 (TA Instruments) at a heating rate of  $10\text{ K min}^{-1}$  in a temperature range between  $50$  and  $350\text{ }^\circ\text{C}$  and with a helium or nitrogen gas flow of  $25\text{ mL min}^{-1}$ .<sup>[67]</sup> Due to gas evolution, the aluminum pan was punctured for the cycled sample.

The powders morphology was investigated by scanning electron microscopy (SEM) using a Carl Zeiss AURIGA field emission microscope with a Schottky field emitter as an electron source and an accelerating voltage of  $3\text{ kV}$  for top-view and  $5\text{ kV}$  for cross-sectional images. Focused ion beam scanning electron microscope (FIB-SEM) milling was performed with milling currents of  $7\text{ nA}$  and  $3\text{ nA}$ ,  $100\text{ pA}$  and  $50\text{ pA}$  for polishing and a FIB acceleration voltage of  $30\text{ kV}$  using a Zeiss cross-beam 340 FIB-SEM.

Secondary particle size distributions and shapes were analyzed by static light scattering and high-speed CCD cameras (Bettersizer S3 Plus, Bettersize Instruments) using deionized water as a solvent and ultrasonic-assisted dispersion. For shape analysis, >5000 particles were taken into account, but as the resolution of the cameras was limited, only particles  $\geq 10 \mu\text{m}$  were included. The cycled sample was previously heated up to  $600^\circ\text{C}$  for 20 min to burn off binder and carbon residues. Measurements were repeated three times.

The powders' specific or Brunauer–Emmet–Teller surface area was investigated by krypton physisorption at  $-196^\circ\text{C}$  on a 3Flex 3500 device (Micromeritics GmbH). Prior to the measurements, powders were degassed at  $120^\circ\text{C}$  ( $100^\circ\text{C}$  for the cycled sample) overnight under reduced pressure with a VacPrep 061 (Micromeritics GmbH). Consistency criteria were applied according to Rouquerol et al. and IUPAC.<sup>[68]</sup>

Tap densities of the powdered samples were determined by tapping  $\approx 2 \text{ g}$  of material within a measuring cylinder 10 000 times using an Autotap tapped density analyzer (Quantachrome Instruments). Measurements were repeated twice.

For the determination of the hydroxide and carbonate contents on the particles' surface, Warden titration was performed using an autotitrator (905 Titrand, Metrohm). Samples were prepared in a nitrogen-filled glove bag by stirring 0.625 g of material for 2 min in 25 mL ultra-pure water (Millipore) and subsequent fast vacuum filtration through a frit. After flushing with argon, 10 mL of the filtrate was added to the titration vessel which was connected air-tightly to the titrator. For the titration,  $0.05 \text{ mol L}^{-1}$  HCl was added at a dynamic dosing rate and under continuous stirring. Equivalence points of the titration were determined as the maxima of the first derivative of the titration curve. Measurements were repeated twice. Warden's titration method was validated for Ni-rich NCMs by Schuer et al.<sup>[38]</sup>

Powder X-ray diffraction measurements (PXRD) were performed with a Stoe STADI P diffractometer in Debye-Scherrer geometry with a Dectris MYTHEN2 1K detector using  $\text{Mo K}_\alpha$  radiation ( $\lambda = 0.7093 \text{ \AA}$ ) and employing a  $\text{Ge}(111)$  monochromator. The diffraction data was collected within an angle range of  $4\text{--}55^\circ$ . All samples were measured in sealed borosilicate glass capillaries (Hilgenberg,  $\varnothing = 0.5 \text{ mm}$ ). Instrumental broadening and asymmetry were determined by measuring a  $\text{LaB}_6$  standard in the same sample configuration. Rietveld refinement was performed using TOPAS 7 and was based on a hexagonal  $\alpha\text{-NaFeO}_2$  structure belonging to the space group  $R\bar{3}m$ . Constraints were added to maintain the sample's stoichiometry determined by ICP-OES. The following parameters were refined: fifth-order background Chebyshev polynomial, scale factor, zero shift, absorption,  $a$  and  $c$  unit cell parameters, crystallite size, micro-strain  $\epsilon_0$ , fractional atomic coordinate of oxygen  $z_{\text{Ox}}$ , occupancy of Ni on Li site, and isotropic displacement parameters  $B$  of O, TM and Li. Errors were reported as the standard deviation  $\sigma$  obtained from Rietveld refinement in TOPAS.

All (scanning) transmission electron microscopy (TEM/STEM) techniques, including high-resolution (HR-)TEM coupled with Fast Fourier Transform (FFT) patterns, bright-field (BF-)STEM, and electron energy loss spectroscopy (EELS-)STEM were performed on an FEI Titan Themis G3 300 TEM equipped with a monochromator, a Gatan Image Filter (GIF) quantum ER/965 P spectrometer, Ceta 16 m camera, and BF image detectors at an accelerating voltage of 300 kV. The EELS spectra were recorded with  $0.25 \text{ eV/channel}$  dispersion and the  $L_3/L_2$  intensity ratio was calculated by using a power law to subtract the background and then considering the positive contribution of the second derivative of the EELS spectra under individual  $L_2$  and  $L_3$  peaks.<sup>[69]</sup> A low electron beam current was used to suppress beam damage of the samples. The TEM samples (lamella) were prepared by FIB-SEM as described above and transferred to TEM using a vacuum transfer holder (Gatan).

Using fluorescence-yield (FY), inverse fluorescence-yield (IFY), and total electron-yield (TEY) detection modes, near-edge X-ray absorption fine structure (NEXAFS) spectra at the Ni  $L_{2,3}$ , Co  $L_{2,3}$ , Mn  $L_{2,3}$ , and O K edges were measured at IQMT's soft X-ray beamline WERA at the KIT Light Source (Karlsruhe, Germany). The energy resolution was set to  $0.2\text{--}0.4 \text{ eV}$ . Data evaluation includes steps such as energy calibration, dark current subtraction, normalization by  $I_0$ , and background removal as described in literature.<sup>[70]</sup>

**Electrode Preparation:** For cathode paste preparation, 3 wt% PVDF binder (Solef 5130, Solvay) was dissolved in *N*-methyl-2-pyrrolidone (NMP, anhydrous, 99.5%, Sigma–Aldrich), then 3 wt% carbon black as conductive agent (Super C65, Imerys Graphite & Carbon) and 94 wt% NCM-831205 ( $\text{LiNi}_{0.83}\text{Co}_{0.12}\text{Mn}_{0.05}\text{O}_2$ , BASF, or its cycled or recycled derivatives) as active material were added, reaching a solid content of 50 wt%. The electrode paste was homogenized by a high-energy disperser (Dissolver Dispermat LC30, VMAGetzmann GmbH) at a speed of 2000 rpm for 5 min, 10 000 rpm for 30 min, and 2000 rpm for 5 min, before coating the dispersion with a doctor-blade (Zehntner GmbH) and an automatic film applicator (Sheen Instruments) on aluminum foil ( $20 \mu\text{m}$ , Nippon foil) which was previously washed with ethanol. The electrode sheets were dried for 2 h at  $80^\circ\text{C}$ , calendered (CLP 2025, Hohsen Corp.) to reach a porosity of  $\approx 35\%$ , punched out in 14 mm discs, and dried in a Büchi B-585 glass drying oven under reduced pressure ( $< 5 \cdot 10^{-2} \text{ bar}$ ) for 12 h at  $120^\circ\text{C}$ . The average active mass loading of the cathode was  $\approx 8.6 \pm 0.5 \text{ mg cm}^{-2}$  for investigations in NCM-831205 || Li metal cells, resulting in areal capacities of  $\approx 1.3 \pm 0.1 \text{ mAh cm}^{-2}$ , based on the practical capacity of NCM-831205 ( $200 \text{ mAh g}^{-1}$  at  $4.3 \text{ V vs Li|Li}^+$ ). For NCM-831205 || graphite lithium ion-cell investigations, the average active material mass loading was  $\approx 18.4 \pm 1.0 \text{ mg cm}^{-2}$ , resulting in areal capacities of  $\approx 2.3 \pm 0.1 \text{ mAh cm}^{-2}$ , based on the second cycle discharge capacity of NCM-831205 || Li metal cells cycled up to  $4.3 \text{ V vs Li|Li}^+$ .

The negative electrodes used for NCM-831205 || graphite lithium ion-cell investigations were produced in-house from the Cell Production Team at the Battery Research Center MEET in Münster, Germany, as described in the SI. Circular electrode disks with  $\varnothing = 15 \text{ mm}$  in diameter were punched out and dried in a Büchi B-585 glass drying oven under reduced pressure ( $< 5 \cdot 10^{-2} \text{ bar}$ ) for 12 h at  $120^\circ\text{C}$ . The average active mass loading of the negative electrodes was  $\approx 13.5 \pm 0.5 \text{ mg cm}^{-2}$ , resulting in an areal capacity of  $\approx 2.6 \pm 0.1 \text{ mAh cm}^{-2}$  based on the practical capacity of graphite ( $\approx 350 \text{ mAh g}^{-1}$ ).

**Cell Assembly and Electrochemical Characterization:** Electrochemical properties were studied in a two-electrode configuration in coin cells (CR2032, Hohsen Corp.) assembled in a dry room. A polymer membrane ( $\varnothing = 16 \text{ mm}$ , Celgard 2500, Celgard) was used as a separator and soaked with  $35 \mu\text{L}$  of LP57 electrolyte (1 M  $\text{LiPF}_6$  in 3:7 vol.% ethylene carbonate/ethyl methyl carbonate, EC/EMC, Solvionic) with 2 wt% vinylene carbonate (VC). For NCM-831205 || Li metal cells, lithium metal foil (battery grade: purity  $\geq 99.9\%$ , China Energy Lithium (CEL Co.)) discs with a diameter of 15 mm and a thickness of  $500 \mu\text{m}$  were used. To avoid Li metal plating at the graphite negative electrode in NCM-831205 || graphite lithium ion-cells, the negative/positive (N/P) capacity balancing ratio was set to 1.15:1.00, based on the second cycle discharge capacities of NCM-831205 || Li metal cells. At least three cells per sample were assembled to ensure reproducibility. The mean and its standard deviation were shown in the corresponding figures.

Constant current (CC) charge/discharge cycling was carried out on a Maccor Series 4000 battery tester (Maccor, Inc.) at  $20^\circ\text{C}$ . For a current rate of 1 C, the specific current was defined as  $200 \text{ mA g}^{-1}$ . The NCM-831205-based cathodes rate capability and high-voltage stability was probed in NCM-831205 || Li metal cells according to the following procedure: 6 h at open-circuit-voltage (OCV), two formation cycles at  $20 \text{ mA g}^{-1}$  (0.1 C), three cycles at  $40 \text{ mA g}^{-1}$  (0.2 C), and five cycles at  $66 \text{ mA g}^{-1}$  (0.33 C),  $100 \text{ mA g}^{-1}$  (0.5 C),  $200 \text{ mA g}^{-1}$  (1 C) and  $600 \text{ mA g}^{-1}$  (3 C) each, two cycles at  $20 \text{ mA g}^{-1}$  (0.1 C) and 15 cycles at  $66 \text{ mA g}^{-1}$  (0.33 C) for different upper cut-off voltages. To reduce heterogeneous Li metal plating on the Li metal negative electrode, the specific current was only varied upon discharge and kept constant during charge at  $20 \text{ mA g}^{-1}$  (0.1 C) for cycles at  $20 \text{ mA g}^{-1}$  during discharge and at  $40 \text{ mA g}^{-1}$  (0.2 C) for all other cycles. The cell voltage window was set between  $4.3/4.4/4.5$  and  $2.9 \text{ V}$ . The long-term cycle life was evaluated in NCM-831205 || graphite lithium ion-cells operated in a cell voltage range of  $4.2\text{--}2.8 \text{ V}$ . After 15 min at  $1.5 \text{ V}$  to prevent Cu current collector dissolution<sup>[71]</sup> and 6 h at OCV, cells were cycled for four cycles at  $20 \text{ mA g}^{-1}$  for interphase formation, followed by cycling at  $200 \text{ mA g}^{-1}$  until reaching 80% of the fifth cycle discharge capacity. Every 100 cycles, cells were cycled twice at  $20 \text{ mA g}^{-1}$ . After each charging step, a constant voltage (CV) step was included

for a maximum of 30 min or until the specific current dropped below 10 mA g<sup>-1</sup>.

## Supporting Information

Supporting Information is available from the Wiley Online Library or from the author.

## Acknowledgements

The authors thank the Federal State of North Rhine-Westphalia for funding the international graduate school BACCARA (Battery Chemistry, Characterization, Analysis, Recycling and Application). The authors thank the Cell Production team at MEET, namely Jonathan Dylong, Gültekin Göl, Andrea Jansen, and Lena Streller, for the production of multilayer pouch cells, Debbie Berghus for performing DSC measurements and Uta Rodehorst for XPS measurements. The authors also thank Andre Bar for his graphical support. The authors are grateful to the KIT Light Source, Karlsruhe, Germany, for the provision of beamtime. Furthermore, the authors would like to thank the Deutsche Forschungsgemeinschaft (DFG) for funding the TEM equipment via the Major Research Instrumentation Program under INST 211/719-1 FUGG and the XRD device under project number 459785385. Crystal structures were visualized by using VESTA (Visualization for Electronic and Structural Analysis).

Open access funding enabled and organized by Projekt DEAL.

## Conflict of Interest

The authors declare no conflict of interest.

## Data Availability Statement

The data that support the findings of this study are available from the corresponding author upon reasonable request.

## Keywords

circular economy, closed loop, direct recycling, lithium ion battery, NCM, solid-state

Received: February 22, 2024

Revised: June 10, 2024

Published online:

- [1] J. Neumann, M. Petranikova, M. Meeus, J. D. Gamarra, R. Younesi, M. Winter, S. Nowak, *Adv. Energy Mater.* **2022**, *12*, 2102917.
- [2] KPMG for Propulsion, Québec **2019**, [https://propulsionquebec.com/wp-content/uploads/2019/09/2019-09-05-Filiere-des-batteries-lithium-ion-Developper-un-secteur-davenir-pour-leconomie-Qc\\_EN.pdf](https://propulsionquebec.com/wp-content/uploads/2019/09/2019-09-05-Filiere-des-batteries-lithium-ion-Developper-un-secteur-davenir-pour-leconomie-Qc_EN.pdf) (accessed: July 2024).
- [3] Regulation (EU) 2023/1542 of the European Parliament and of the Council of 12 July 2023 concerning batteries and waste batteries, amending Directive 2008/98/EC and Regulation (EU) 2019/1020 and repealing Directive 2006/66/EC (Text with EEA relevance), **2023**, <https://eur-lex.europa.eu/eli/reg/2023/1542/oj> (accessed: July 2024).
- [4] A. Kwade, J. Diekmann, *Recycling of lithium-ion batteries. The LithoRec way*, Springer, Cham, Switzerland **2018**.
- [5] S. Krüger, C. Hanisch, A. Kwade, M. Winter, S. Nowak, *J. Electroanal. Chem.* **2014**, *726*, 91.
- [6] L. Gaines, Y. Wang, *Electrochem. Soc. Interface* **2021**, *30*, 51.
- [7] L. Gaines, Q. Dai, J. T. Vaughey, S. Gillard, *Recycling* **2021**, *6*, 31.
- [8] a) B. E. Murdock, K. E. Toghill, N. Tapia-Ruiz, *Adv. Energy Mater.* **2021**, *11*, 2102028; b) Y. Lu, K. Peng, L. Zhang, *ACS EST Engg* **2022**, *2*, 586; c) X. Yu, W. Li, V. Gupta, H. Gao, D. Tran, S. Sarwar, Z. Chen, *Global Challenges* **2022**, *6*, 2200099.
- [9] L. Lander, T. Cleaver, M. A. Rajaeifar, V. Nguyen-Tien, R. J. R. Elliott, O. Heidrich, E. Kendrick, J. S. Edge, G. Offer, *iScience* **2021**, *24*, 102787.
- [10] a) P. Xu, Q. Dai, H. Gao, H. Liu, M. Zhang, M. Li, Y. Chen, K. An, Y. S. Meng, P. Liu, Y. Li, J. S. Spangenberg, L. Gaines, J. Lu, Z. Chen, *Joule* **2020**, *4*, 2609; b) X. Liu, M. Wang, L. Deng, Y.-J. Cheng, J. Gao, Y. Xia, *Ind. Eng. Chem. Res.* **2022**, *61*, 3831; c) Z. Jiang, J. Sun, P. Jia, W. Wang, Z. Song, X. Zhao, Y. Mao, *Sustainable Energy Fuels* **2022**, *6*, 2207; d) S. E. Sloop, M. Allen, US9484606 (B1), **2014**; e) S. E. Sloop, US2014377597 (A1), **2014**.
- [11] H. Wang, S. Burke, R. Yuan, J. F. Whitacre, *J. Energy Storage* **2023**, *60*, 106616.
- [12] a) H. Gao, Q. Yan, P. Xu, H. Liu, M. Li, P. Liu, J. Luo, Z. Chen, *ACS Appl. Mater. Interfaces* **2020**, *12*, 51546; b) H. Wang, J. F. Whitacre, *Energy Technol.* **2018**, *6*, 2429; c) C. Wu, M. Xu, C. Zhang, L. Ye, K. Zhang, H. Cong, L. Zhuang, X. Ai, H. Yang, J. Qian, *Energy Storage Mater.* **2023**, *55*, 154.
- [13] S. E. Sloop, EP3178127 (A1), **2015**.
- [14] Y. Shi, G. Chen, F. Liu, X. Yue, Z. Chen, *ACS Energy Lett.* **2018**, *3*, 1683.
- [15] X. Yu, S. Yu, Z. Yang, H. Gao, P. Xu, G. Cai, S. Rose, C. Brooks, P. Liu, Z. Chen, *Energy Storage Mater.* **2022**, *51*, 54.
- [16] S. E. Sloop, L. Crandon, M. Allen, M. M. Lerner, H. Zhang, W. Sirisaksoontorn, L. Gaines, J. Kim, M. Lee, *Sustainable Mater. Technol.* **2019**, *22*, e00113.
- [17] Z. Qin, T. Zhang, X. Gao, W. Luo, J. Han, B. Lu, J. Zhou, G. Chen, *Adv. Mater.* **2024**, *36*, 2307091.
- [18] a) Z. Qin, Y. Zhang, W. Luo, T. Zhang, T. Wang, L. Ni, H. Wang, N. Zhang, X. Liu, J. Zhou, G. Chen, *Angew. Chem.* **2023**, *62*, 202218672; b) T. Wang, H. Luo, J. Fan, B. P. Thapaliya, Y. Bai, I. Belharouak, S. Dai, *iScience* **2022**, *25*, 103801.
- [19] C. Xu, Q. Dai, L. Gaines, M. Hu, A. Tukker, B. Steubing, *Commun. Mater.* **2020**, *1*, 99.
- [20] H.-J. Noh, S. Youn, C. S. Yoon, Y.-K. Sun, *J. Power Sources* **2013**, *233*, 121.
- [21] J. Kasnatscheew, S. Röser, M. Börner, M. Winter, *ACS Appl. Energy Mater.* **2019**, *2*, 7733.
- [22] T. Li, X.-Z. Yuan, L. Zhang, D. Song, K. Shi, C. Bock, *Electrochem. Energy Rev.* **2020**, *3*, 43.
- [23] S. Klein, P. Bärman, O. Fromm, K. Borzutzki, J. Reiter, Q. Fan, M. Winter, T. Placke, J. Kasnatscheew, *J. Mater. Chem. A* **2021**, *9*, 7546.
- [24] P. Xu, D. H. S. Tan, B. Jiao, H. Gao, X. Yu, Z. Chen, *Adv. Funct. Mater.* **2023**, *33*, 2213168.
- [25] B. Ying, J. R. Fitzpatrick, Z. Teng, T. Chen, T. W. B. Lo, V. Siozios, C. A. Murray, H. E. A. Brand, S. Day, C. C. Tang, R. S. Weatherup, M. Merz, P. Nagel, S. Schuppler, M. Winter, K. Kleiner, *Chem. Mater.* **2023**, *35*, 1514.
- [26] A. Gomez-Martin, F. Reissig, L. Frankenstein, M. Heidebüchel, M. Winter, T. Placke, R. Schmich, *Adv. Energy Mater.* **2022**, *12*, 2103045.
- [27] a) H. Li, A. Liu, N. Zhang, Y. Wang, S. Yin, H. Wu, J. R. Dahn, *Chem. Mater.* **2019**, *31*, 7574; b) H.-H. Ryu, K.-J. Park, C. S. Yoon, Y.-K. Sun, *Chem. Mater.* **2018**, *30*, 1155.
- [28] W. Li, H. Y. Asl, Q. Xie, A. Manthiram, *J. Am. Chem. Soc.* **2019**, *141*, 5097.
- [29] F. Reissig, J. Ramirez-Rico, T. J. Placke, M. Winter, R. Schmich, A. Gomez-Martin, *Batteries* **2023**, *9*, 245.
- [30] S.-M. Bak, E. Hu, Y. Zhou, X. Yu, S. D. Senanayake, S.-J. Cho, K.-B. Kim, K. Y. Chung, X.-Q. Yang, K.-W. Nam, *ACS Appl. Mater. Interfaces* **2014**, *6*, 22594.
- [31] R. M. German, *Crit. Rev. Solid State Mater. Sci.* **2010**, *35*, 263.

- [32] S. Ahmed, A. Pokle, S. Schweidler, A. Beyer, M. Bianchini, F. Walther, A. Mazilkin, P. Hartmann, T. Brezesinski, J. Janek, K. Volz, *ACS Nano* **2019**, *13*, 10694.
- [33] F. Friedrich, B. Strehle, A. T. S. Freiberg, K. Kleiner, S. J. Day, C. Erk, M. Piana, H. A. Gasteiger, *J. Electrochem. Soc.* **2019**, *166*, A3760.
- [34] S. R. Challa, A. T. Delariva, T. W. Hansen, S. Helveg, J. Sehested, P. L. Hansen, F. Garzon, A. K. Datye, *J. Am. Chem. Soc.* **2011**, *133*, 20672.
- [35] M. Müller, L. Schneider, N. Bohn, J. R. Binder, W. Bauer, *ACS Appl. Energy Mater.* **2021**, *4*, 1993.
- [36] R. Jung, R. Morasch, P. Karayaylali, K. Phillips, F. Maglia, C. Stinner, Y. Shao-Horn, H. A. Gasteiger, *J. Electrochem. Soc.* **2018**, *165*, A132.
- [37] S. E. Renfrew, B. D. McCloskey, *J. Am. Chem. Soc.* **2017**, *139*, 17853.
- [38] A. R. Schuer, M. Kuenzel, S. Yang, M. Kosfeld, F. Mueller, S. Passerini, D. Bressler, *J. Power Sources* **2022**, *525*, 231111.
- [39] Y. Duan, L. Yang, M.-J. Zhang, Z. Chen, J. Bai, K. Amine, F. Pan, F. Wang, *J. Mater. Chem. A* **2019**, *7*, 513.
- [40] a) K. Xu, *Chem. Rev.* **2004**, *104*, 4303; b) B. Streipert, L. Stolz, G. Homann, P. Janßen, I. Cekic-Laskovic, M. Winter, J. Kasnatscheew, *ChemSusChem* **2020**, *13*, 5301.
- [41] D. Pritzl, T. Teufl, A. T. S. Freiberg, B. Strehle, J. Sicklinger, H. Sommer, P. Hartmann, H. A. Gasteiger, *J. Electrochem. Soc.* **2019**, *166*, A4056.
- [42] a) D. Mohanty, H. Gabrisch, *J. Power Sources* **2012**, *220*, 405; b) M. S. Whittingham, *Chem. Rev.* **2004**, *104*, 4271.
- [43] J. Kasnatscheew, M. Evertz, R. Kloepsch, B. Streipert, R. Wagner, I. Cekic Laskovic, *Mater. Energy Technol.* **2017**, *5*, 1670.
- [44] J. Kasnatscheew, R. Wagner, M. Winter, I. Cekic-Laskovic, *Top. Curr. Chem.* **2018**, *376*, 16.
- [45] P. Kurzahls, F. Riewald, M. Bianchini, H. Sommer, H. A. Gasteiger, J. Janek, *J. Electrochem. Soc.* **2021**, *168*, 110518.
- [46] H. Ronduda, M. Zybert, A. Szczęśna-Chrzan, T. Trzeciak, A. Ostrowski, D. Szymański, W. Wieczorek, W. Raróg-Pilecka, M. Marcinek, *Nanomaterials* **2020**, *10*, 2018.
- [47] J. Zhu, S. Sharifi-Asl, J. C. Garcia, H. H. Iddir, J. R. Croy, R. Shahbazian-Yassar, G. Chen, *ACS Appl. Energy Mater.* **2020**, *3*, 4799.
- [48] B. Huang, D. Liu, K. Qian, L. Zhang, K. Zhou, Y. Liu, F. Kang, B. Li, *ACS Appl. Mater. Interfaces* **2019**, *11*, 14076.
- [49] K. Kleiner, C. A. Murray, C. Grosu, B. Ying, M. Winter, P. Nagel, S. Schuppler, M. Merz, *J. Electrochem. Soc.* **2021**, *168*, 120533.
- [50] K. Kleiner, B. Ying, Z. Teng, M. Avdeev, A. Senyshyn, J. Peng, S. B. Simonsen, O. Dolotko, R. Schmuch, S. Indris, M. Merz, P. Nagel, S. Schuppler, H. Ehrenberg, M. Winter, **2023**, PREPRINT (Version 1) available at Research Square, <https://doi.org/10.21203/rs.3.rs-3498657/v1>.
- [51] C. Tian, D. Nordlund, H. L. Xin, Y. Xu, Y. Liu, D. Sokaras, F. Lin, M. M. Doeff, *J. Electrochem. Soc.* **2018**, *165*, A696.
- [52] a) A. Jetybayeva, N. Schön, J. Oh, J. Kim, H. Kim, G. Park, Y.-G. Lee, R.-A. Eichel, K. Kleiner, F. Hausen, S. Hong, *ACS Appl. Energy Mater.* **2022**, *5*, 1731; b) F. Hausen, N. Scheer, B. Ying, K. Kleiner, *Electrochem. Sci. Adv.* **2023**, 2300017.
- [53] a) D. M. Pease, S. D. Bader, M. B. Brodsky, J. I. Budnick, T. I. Morrison, N. J. Zaluzec, *Phys. Lett. A* **1986**, *114*, 491; b) Z. L. Wang, J. Bentley, N. D. Evans, *Micron* **2000**, *31*, 355.
- [54] a) H. Liu, M. Bugnet, M. Z. Tessaro, K. J. Harris, M. J. R. Dunham, M. Jiang, G. R. Goward, G. A. Botton, *Phys. Chem. Chem. Phys.* **2016**, *18*, 29064; b) L. Zou, Z. Liu, W. Zhao, H. Jia, J. Zheng, Y. Yang, G. Wang, J.-G. Zhang, C. Wang, *Chem. Mater.* **2018**, *30*, 7016.
- [55] H. Li, N. Zhang, J. Li, J. R. Dahn, *J. Electrochem. Soc.* **2018**, *165*, A2985.
- [56] J. Kasnatscheew, U. Rodehorst, B. Streipert, S. Wiemers-Meyer, R. Jakelski, R. Wagner, I. C. Laskovic, M. Winter, *J. Electrochem. Soc.* **2016**, *163*, A2943.
- [57] N. A. Chernova, G. M. Nolis, F. O. Omenya, H. Zhou, Z. Li, M. S. Whittingham, *J. Mater. Chem.* **2011**, *21*, 9865.
- [58] Y. Bi, T. Wang, M. Liu, R. Du, W. Yang, Z. Liu, Z. Peng, Y. Liu, D. Wang, X. Sun, *RSC Adv.* **2016**, *6*, 19233.
- [59] T. Waldmann, A. Iturrondobeitia, M. Kasper, N. Ghanbari, F. Aguesse, E. Bekaert, L. Daniel, S. Genies, I. J. Gordon, M. W. Löble, E. De Vito, M. Wohlfahrt-Mehrens, *J. Electrochem. Soc.* **2016**, *163*, A2149.
- [60] a) J. Kasnatscheew, M. Evertz, B. Streipert, R. Wagner, R. Klöpsch, B. Vortmann, H. Hahn, S. Nowak, M. Amereller, A.-C. Gentschev, P. Lamp, M. Winter, *Phys. Chem. Chem. Phys.* **2016**, *18*, 3956; b) S.-H. Kang, W.-S. Yoon, K.-W. Nam, X.-Q. Yang, D. P. Abraham, *J. Mater. Sci.* **2008**, *43*, 4701; c) Z. Chi, J. Li, L. Wang, T. Li, Y. Wang, Y. Zhang, S. Tao, M. Zhang, Y. Xiao, Y. Chen, *Green Chem.* **2021**, *23*, 9099.
- [61] a) B. J. Ross, M. LeResche, D. Liu, J. L. Durham, E. U. Dahl, A. L. Lipson, *ACS Sustainable Chem. Eng.* **2020**, *8*, 12511; b) E. Antolini, *Phys. Status Solidi A* **1999**, *173*, 357; c) E. McCalla, G. H. Carey, J. R. Dahn, *Solid State Ionics* **2012**, *219*, 11.
- [62] K. Park, B. Choi, *J. Alloys Compd.* **2018**, *766*, 470.
- [63] a) E. B. Abebe, C.-C. Yang, S.-H. Wu, W.-C. Chien, Y.-J. Li, *ACS Appl. Energy Mater.* **2021**, *4*, 14295; b) J. Choi, A. Manthiram, *Electrochem. Solid-State Lett.* **2004**, *7*, A365.
- [64] X. Xiong, Z. Wang, P. Yue, H. Guo, F. Wu, J. Wang, X. Li, *J. Power Sources* **2013**, *222*, 318.
- [65] B. Vortmann-Westhoven, M. Winter, S. Nowak, *J. Power Sources* **2017**, *346*, 63.
- [66] M. Evertz, J. Kasnatscheew, M. Winter, S. Nowak, *Anal. Bioanal. Chem.* **2019**, *411*, 277.
- [67] Y. P. Stenzel, M. Börner, Y. Preibisch, M. Winter, S. Nowak, *J. Power Sources* **2019**, *433*, 226709.
- [68] a) J. Rouquerol, P. Llewellyn, F. Rouquerol in *Studies in Surface Science and Catalysis: Characterization of Porous Solids VII* (Eds.: P. L. Llewellyn, F. Rodriguez-Reinoso, J. Rouquerol, N. Seaton), Elsevier, Amsterdam and Oxford **2007**; b) M. Thommes, K. Kaneko, A. V. Neimark, J. P. Olivier, F. Rodriguez-Reinoso, J. Rouquerol, K. S. Sing, *Pure Appl. Chem.* **2015**, *87*, 1051.
- [69] a) T. Riedl, T. Gemming, K. Wetzig, *Ultramicroscopy* **2006**, *106*, 284; b) F. Cosandey, D. Su, M. Sina, N. Pereira, G. G. Amatucci, *Micron* **2012**, *43*, 22.
- [70] a) M. Merz, P. Nagel, C. Pinta, A. Samartsev, H. v. Löhneysen, M. Wissinger, S. Uebe, A. Assmann, D. Fuchs, S. Schuppler, *Phys. Rev. B* **2010**, *82*, 174416; b) M. Merz, D. Fuchs, A. Assmann, S. Uebe, H. v. Löhneysen, P. Nagel, S. Schuppler, *Phys. Rev. B* **2011**, *84*, 14436.
- [71] B. R. Long, S. G. Rinaldo, K. G. Gallagher, D. W. Dees, S. E. Trask, B. J. Polzin, A. N. Jansen, D. P. Abraham, I. Bloom, J. Bareño, J. R. Croy, *J. Electrochem. Soc.* **2016**, *163*, A2999.